Accepted Manuscript

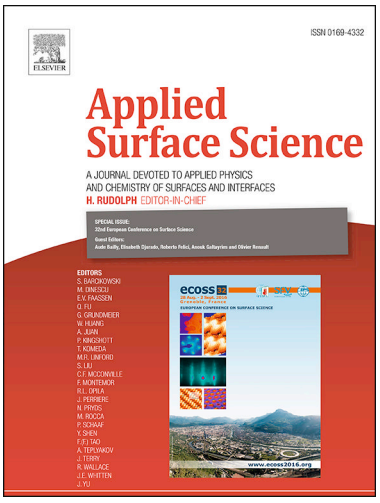

Full Length Article

WO_3 Nanofibrous Backbone Scaffolds for Enhanced Optical Absorbance and Charge Transport in Metal Oxide (Fe_2O_3, $BiVO_4$) Semiconductor Photoanodes towards Solar Fuel Generation

Junghyun Choi, Taeseup Song, Jiseok Kwon, Sangkyu Lee, Hyungkyu Han, Nithish Roy, Chiaki Terashima, Akira Fujishima, Ungyu Paik, Sudhagar Pitchaimuthu

PII: S0169-4332(18)30854-7
DOI: https://doi.org/10.1016/j.apsusc.2018.03.167
Reference: APSUSC 38915

To appear in: *Applied Surface Science*

Received Date: 13 September 2017
Revised Date: 28 January 2018
Accepted Date: 21 March 2018

Please cite this article as: J. Choi, T. Song, J. Kwon, S. Lee, H. Han, N. Roy, C. Terashima, A. Fujishima, U. Paik, S. Pitchaimuthu, WO_3 Nanofibrous Backbone Scaffolds for Enhanced Optical Absorbance and Charge Transport in Metal Oxide (Fe_2O_3, $BiVO_4$) Semiconductor Photoanodes towards Solar Fuel Generation, *Applied Surface Science* (2018), doi: https://doi.org/10.1016/j.apsusc.2018.03.167

WO_3 Nanofibrous Backbone Scaffolds for Enhanced Optical Absorbance and Charge Transport in Metal Oxide (Fe_2O_3, $BiVO_4$) Semiconductor Photoanodes towards Solar Fuel Generation

Junghyun Choi,[a] Taeseup Song,[a*] Jiseok Kwon,[a] Sangkyu Lee,[b] Hyungkyu Han,[b] Nithish Roy,[c] Chiaki Terashima,[c] Akira Fujishima,[c] Ungyu Paik[a,] and Sudhagar Pitchaimuthu[d,*]

[a] *Department of Energy Engineering, Hanyang University, 222 Wangsimni-ro, Seongdong-gu, Seoul 04763, Korea*

[b] *Department of Materials Science and Engineering, Hanyang University, 222 Wangsimni-ro, Seongdong-gu, Seoul 04763, Korea*

[c] *Photocatalysis International Research Center, Research Institute for Science & Technology, Tokyo University of Science, 2641 Yamazaki, Noda, Chiba 278-8510, Japan.*

[d] *Multifunctional Photocatalyst and Coating Lab, SPECIFIC, Materials Research Center, College Engineering, Swansea University (Bay Campus), Swansea, UK*

* Corresponding author: tssong@hanyang.ac.kr (TS); S.Pitchaimuthu@swansea.ac.uk (SP)

Abstract:

Producing clean fuel (O_2 and H_2) using semiconductors through solar driven water splitting process has been considered as a promising technology to mitigate the existing environmental issues. Unlike the conventional single photoabsorbers, heterostructured semiconductors exhibit the merits of improved solar light photon harvesting and rapid charge separation, which are anticipated to result in high quantum yield of solar fuel generation in photoelectrochemical (PEC) cells. In this report, we demonstrate the electrospun derived WO_3 backbone fibrous channel as heteropartner to the primary photoabsorber (Fe_2O_3 and $BiVO_4$) for promoting the electron transport from charge injection point to charge collector as well as photoholes to the electrolyte. We examine structure, optical, photoelectrochemical and charge transfer property of Fe_2O_3/WO_3 and $BiVO_4/WO_3$ electrodes. These results were compared with directly coated Fe_2O_3 and $BiVO_4$ photoabsorber onto conducting substrate without WO_3 backbone. The optical results showed that the absorbance and visible light activity of Fe_2O_3 and $BiVO_4$ is significantly improved by WO_3 backbone fibers due to high amount of photo absorber loading. In addition, one dimensional (1-D) WO_3 fibers beneficially enhance the optical path length to the photoanode through light scattering mechanism. The electrochemical impedance analysis exhibits WO_3 nanofiber backbone reduces charge transfer resistance at Fe_2O_3 and $BiVO_4$ by rapid charge collection and charge separation compare to backbone-free Fe_2O_3 and $BiVO_4$. As a result, Fe_2O_3/WO_3 and $BiVO_4/WO_3$ fibrous hetero interface structures showed fourfold higher photocurrent generation from PEC cell.

Keywords: Photoelectrocatalyst, WO3 fiber, Fe2O3, BiVO4, Electrochemical impedance; Solar fuel

1. Introduction:

Photoelectrochemical (PEC) technique is promising and attracts a great deal of attention in several applications such as water splitting fuel generation, [1, 2], solar rechargeable battery, [3] chemical synthesis, [4, 5] organic pollutant degradation, [6, 7] and biosensing [8, 9]. Typically, a photoactive semiconductor or molecular sensitizer are utilized as oxidation catalyst in the PEC process. The photoirradiated semiconductor produces photocharge carriers such as electron (e^-) and holes (h^+), which are separated and transport to the respective terminals of cathode and electrolyte by applying a small electric potential from outside. The kinetic energy of photoholes at the valence band of semiconductor will drive oxidation process at electrode/electrolyte interfaces. In general, the valence band energy position of semiconductor in the photoanode should lie higher than that of water oxidization potential (Eg> 1.2 V vs RHE) to drive the PEC water oxidation process [10]. Titanium dioxide (TiO_2) is one of the well documented PEC oxidation materials as it possesses appropriate VB position towards water oxidation, excellent chemical stability and photocatalytic activity. However, their UV activated band gap energy (Eg~3.2 eV) is inadequate to demonstrate the solar light driven PEC process as it absorbs only 5% light photons from visible light region [11]. As a consequence, narrow band gap energy semiconductor materials are proposed to replace the TiO_2 in solar light driven PEC oxidation process. Recently, hematite (Fe_2O_3) [12-16], and bismuth vanadate ($BiVO_4$) [17-19] perceived profound attention in visible light driven water oxidation process. It is well known that the thickness of the photoabsorber coating (photoanode) dictates light absorbance quantity. But, the short hole diffusion length characteristics of Fe_2O_3 (2- 4 nm) [20] and $BiVO_4$ (60-200 nm) [21, 22] at electrode/electrolyte interface could limit the thickness of the photoanode as well affect the surface-mediated and/or internal electron/hole recombination

and thus, could ultimately affect PEC efficiency.

To promote the charge separation rate at semiconductor/electrolyte interfaces, multiple routes were proposed on semiconductor modification through a) metal carriers doping [23, 24], b) co-catalyst decoration [25], c) hetero partner assembly [26] and d) inserting interfacial layer [27]. Mostly, these protocols facilitate the charge separation at Fe_2O_3 and $BiVO_4$ layers through passivating the surface states, and grain boundaries responsible for charge recombination at electrode/electrolyte interfaces [28-31]. However, overcoming the photoanode thickness dependent hole-transport still remains a great challenge. Instead of coating the photoelectrocatalyst layer (guest) directly onto the substrates, it is anticipated that assembling onto nanoscale, wide-pore structured backbone scaffold (host) that are spatially connected to the substrate could simultaneously improve the charge collection and charge transport at guest layer/electrolyte interfaces [32]. In this line, we are demonstrating tungsten oxide (WO_3) as an appropriate backbone scaffold choice for the Fe_2O_3 and $BiVO_4$ guest layers as its conduction band is lower than these materials. Sivula et al [33] demonstrated that Fe_2O_3 guest layer coated onto WO_3 nanostructured host scaffold showed effective charge separation than directly coated Fe_2O_3 onto substrate. On the other hand, $BiVO_4$ primary photoabsorber shell layer coated WO_3 nanowire backbone layer markedly enhanced the charge separation at $BiVO_4$/electrolyte interfaces [34]. In literature, similar type of WO_3 backbone scaffold has been progressed in the form of nanotube, inverse opal, and nanowire [35, 36]. Mostly, the demonstrated WO_3 scaffold structures in the literature exhibits limited pore-size (5-10 nm), which may be inadequate in either producing homogenous guest photoabsorber coating or sufficient space availability for the electrolyte percolation at the electrode surface.

Here we propose highly interconnected, wide-pore structured electrospun WO_3 nanofibers as a backbone scaffold for Fe_2O_3 and $BiVO_4$ guest layers coating. Compared to

the vacuum based physical techniques, the electrospinning technique is simple, economic and displays large scale viability. For instance, 1-D nanostructures prepared through chemical vapor deposition, and VLS growth technique required sophisticated environment including high temperature processing, high purity of chemical precursor, and long processing duration. In the case of anodization technique, it has major limitation on assembling 1-D nanostructures on metal substrates only. In this view, electrospining process is a simple route for assembling 1-D nanostructures. It can be operated at room temperature, less processing time and readily collected onto substrates.

To the best of our knowledge, for the first time, systematically prepared Fe_2O_3 and $BiVO_4$ coating onto WO_3 fibers as illustrated in **Figure 1** is demonstrated in solar fuel generation. Identical amount of precursor is loaded onto both FTO substrate (**Figure 1a**) and WO_3 fibers coated FTO substrates (**Figure 1b**). Subsequently, these samples were sintered at 500 °C, and thus formed thin conformal guest layer coating. In view of light penetration at different portion of the photoanode (top and bottom layer) the photocharge carrier separation from guest layer to electrolyte and substrate seems to be different. For instance, in the case of direct coating protocol (**Figure 1a**), the photoholes transport distance (indicated as x_2 in Figure 1a) from closer to the electrolyte position is efficient than underneath layer position (indicated as $x_1$in **Figure 1a**). At WO_3 scaffold based protocol (**Figure 1b**), the photoelectrons from guest layer is radially transport to the charge collector, thus hole transport distance from guest layer to the electrolyte is approximately identical ($x_1 = x_2$). Therefore, regardless of the light penetration position the photoholes can passage to the electrolyte efficiently. The structure, optical, electrochemical and PEC properties are systematically examined, which reveals the advantage of WO_3 backbone scaffold towards improving the charge separation and charge transport at guest photoelectrocatalyst/electrolyte interface in water oxidation reactions.

2. Experimental

2a. WO_3 nanofibrous electrode fabrication: WO_3 nanofiber (NF) layer was fabricated by electrospinning method. 0.6 g of tungsten (VI) ethoxide (Alfa Aesar) was solved in 2.5 mL of N,N-dimethylformamide (99.8%, Sigma Aldrich) and sonicated for 30 min. And then, 0.15 g of acetic acid (99.5%, Samchun Chemical) and 0.5 g of poly(vinyl acetate) (Mw ~500,000, Sigma Aldrich) were mixed with the solution and stirred overnight. The NFs were electrospun onto the pre-cleaned fluorinated tin oxide (FTO) substrates using the resulted solution at a DC voltage of 20 kV with a flow of 0.2 ml/h. Finally, the as-spun nanofiber layer was annealed at 500 ^{o}C for 3 h in air. In order to overcome the fibrous films peel off from substrate during sintering process, the WO_3 fiber films were kept under hot press technique at 100 ℃ for 2 minutes. During the hot pressing pre-treatment, the PVA polymer binder was melted and facilitate the WO_3 fibers attached onto substrate.

2b. Synthesis of the $BiVO_4$ and Fe_2O_3 layer: The coating solution of $BiVO_4$ was prepared as follows: 0.1462 g of ammonium metavanadate (99%, Sigma Aldrich), 0.6061 g of bismuth nitrate pentahydrate (98%, Sigma Aldrich), 0.4803 g of citric acid (anhydrous, Sigma Aldrich), and 0.825 g of nitric acid (60%, Daejung Chemical) were mixed into 2.925 mL of distilled water. For the Fe_2O_3 solution, 0.505 g of iron nitrate nonahydrate (98%, Sigma Aldrich), 0.4803 g of citric acid (anhydrous, Sigma Aldrich), and 0.825 g of nitric acid (60%, Daejung Chemical) were dissolved in 2.925 mL of distilled water. The $BiVO_4$ layer and Fe_2O_3 layers were formed by spin-coating the solutions at 2000 rpm for 30s onto WO_3 nanofiber layer, followed by annealing at 500 ^{o}C for 3 h in air. To compare the photoanode performance of $BiVO_4$ and Fe_2O_3 in the presence and absence of WO_3 backbone fiber in the PEC cells, similar quantity of $BiVO_4$ and Fe_2O_3 precursor solution as is explained above was coated onto FTO directly. The resultant films were annealing at 500 ^{o}C for 3 h in air.

2c. Characterization: The crystalline structure of electrospun WO_3 film was studied using an X-ray diffractometer (XRD, New D8 Advance, Bruker). The surface morphology of the semiconductor films was analyzed by field emission scanning microscopy (FESEM, JSM-7600F, JEOL. The heterostructure formation at $BiVO_4/WO_3$ sample was analyzed by high resolution transmission electron microscopy (JEM-2100F, JEOL). The optical absorbance spectra of the resultant semiconductor films were recorded using a UV-Vis spectrophotometer (V670, JASCO) in the diffuse reflectance mode. Note that, the incident light beam was allowed through the substrate side.

2d. Photoelectrochemical studies: The photoelectrochemical measurements were carried out using an FRA-equipped potentiostat (PGSTAT 302N, Autolab). The standard three-electrode configuration encompass with semiconductor layers coated onto FTO glass as the working electrode, Ag/AgCl reference electrode and a platinum foil counter electrode were used in these experiments. The photoelectrochemical performance was evaluated using a 0.5 M Na_2SO_4 aqueous solution-based electrolyte. The pH of the solution was 6. Prior to the PEC experiments, the electrolyte was purged with nitrogen gas for 30 min. A 300 W Xe lamp (6258, Newport) with AM 1.5 and an IR cut filter was used as the light source. The current was recorded from PEC cell under chronoamperometric mode at constant applied potential 0.7 V Vs Ag/AgCl. At the consecutive light on/off cycles, respective output current was recorded. The electrochemical impedance spectroscopy (EIS) was used to examine the charge transfer characteristics of the electrode/electrolyte interfaces. The Nqyuist plots were recorded in the frequency range between 0.1 Hz–100 kHz at an amplitude of 20 mV using a potentiostat (PGSTAT 302N, Autolab).

3. Results and discussion

The X-ray diffraction (XRD) pattern of as-synthesized electrospun WO_3 membrane onto FTO substrate is presented in **Figure 1a**. The significant peaks appearing at 23.1°, 23.6°, and 24.4° correspond to the (002), (020), and (200) planes of monoclinic WO_3, respectively (JCPDS 01-083-0950). Other significant peaks at 33.6°, 37.5° and 51.1° represents (202), (103) and (114) crystalline planes of WO_3 [37, 38] [27] . The $BiVO_4$ film coated onto FTO substrate showed monoclinic scheelite crystalline structure (PDF 00-014-0688). In this sample, strong crystalline peaks observed at 28.4 °, 30.8 ° and 50.5 ° corresponds to (-130), (040), and (202) crystalline planes of monoclinic scheelite structure[39]. The Fe_2O_3 thin film coated onto FTO conducting substrate, the crystalline peaks of FTO (indicated as *) is dominated than Fe_2O_3. However, a small peak exhibits at 54.1° endorse the (116) crystalline phase of hematite structure (JCPDS- 01-086-0550). In the case of $BiVO_4$ and Fe_2O_3 layer coated onto WO_3 fibers, similar crystalline peaks were observed as is in the backbone-free films. These results ensure the post deposition of $BiVO_4$ and Fe_2O_3 layer and sustain their growth on WO_3 fiber surface.

The surface morphology of the Fe_2O_3, $BiVO_4$ and WO_3 thin films coated onto FTO substrates are presented in **Figure 3 (a) – (c)**. From **Figure 3 (a)**, the Fe_2O_3 film exhibits thin layer growth and strong features of FTO quasi crystals is observed in the background. In the case of $BiVO_4$ thin films, it shows mosaic morphology with pores formation around grain boundaries. The similar porous $BiVO_4$ films is reported by other researchers [40-42]. The **Figure 3 (c)** SEM image of electrospun WO_3 sample reveals highly interconnected fibrous channels with ~100-150 nm diameter. In between the WO_3 fibrous channel ample room is available for growing Fe_2O_3 and $BiVO_4$ thin films. As is expected, the **Figure 3 (d) and (e)** shows that the WO_3 fibrous surface is completely filled with Fe_2O_3 and $BiVO_4$. It implies that WO_3 backbone fiber scaffold enhance film integrity of Fe_2O_3 and $BiVO_4$ coating compared to their individual films coating directly onto FTO substrates. In order to ensure the

Fe_2O_3 and $BiVO_4$ formation onto WO_3 fibers, elemental mapping analysis is carried out and the corresponding results were presented in **Figure S1** and **S2** (See supporting information). The Fe and O constitutes from **Figure S1**, as well as Bi, V, and O species observed from **Figure S2** endorse the formation of Fe_2O_3 and $BiVO_4$ films onto WO_3 fibers. Further, ensure the heterostruture formation at primary photoabsorber coated WO_3 backbone fiber, we randomly analyze $BiVO_4/WO_3$ sample using high resolution transmission electron microscopy (HRTEM). The **Figure 4** shows the HRTEM image of $BiVO_4/WO_3$ sample. From **Figure 4 (a)**, the primary photoabsorber of $BiVO_4$ is completely covered as thin layer onto WO_3 fiber surface. Further examining at 10 nm scale (**Figure 4 (b)**), a thin layer of $BiVO_4$ is coated onto (002) crystalline phase of WO_3 fiber surface. These results are in line with XRD and elemental mapping results on $BiVO_4/WO_3$ composite.

The optical absorption spectrum of Fe_2O_3 and $BiVO_4$ films in the presence and absence of WO_3 backbone nanofiber is presented in **Figure 5a**. The onset light absorbance at backbone-free Fe_2O_3 and $BiVO_4$ films are found to be at around ~590 nm, and ~490 nm, respectively. Though, similar quantity of Fe_2O_3 and $BiVO_4$ precursor coated onto WO_3 fiber compared to direct coating onto substrate as depicted in **Scheme 1**, the resultant optical absorbance of Fe_2O_3 and $BiVO_4$ is strikingly enhanced (**Figure 5a**) at visible light wavelength. The optical absorbance of Fe_2O_3 is enhanced in the regions between ~340 and 535 nm by WO_3 fiber. In the case of $BiVO_4$ films, the onset light absorbance is shifted from 470 nm to ~480 nm. This might be attributed to the improvement of $BiVO_4$ crystal growth on WO_3 fiber surface compare to direct growth onto substrate. Overall, the backbone WO_3 fiber (host) promotes the light absorbance of Fe_2O_3 and $BiVO_4$ (guest) at visible light wavelength due to high quantity of loading. For instance, optical absorption quantity of single coating cycle of Fe_2O_3 and $BiVO_4$ films onto WO_3 fiber is slightly higher than that of three coating cycles of individual Fe_2O_3 and $BiVO_4$ films onto FTO substrate (**Figure S3**, see supporting

information). Similar optical absorbance enhancement is observed at WO_3 based heterostructured semiconductors by other researchers [34, 43, 44]. One of the other plausible reasons for light absorbance enhancement is multiple light scattering contributed from one dimensional WO_3 fibers. From optical reflectance spectra (**Figure 5b**), it is understood that ~55% of input light is reflected by WO_3 fibers which enhance the optical path length at photoanode. The light scattering from backbone fiber to the primary photoabsorber Fe_2O_3 and $BiVO_4$ may facilitate more photocharge carrier generation towards photoelectrochemical reaction.

To understand the role of WO_3 backbone fiber in charge separation of photocharge carriers at primary Fe_2O_3 and $BiVO_4$ photoabsorber layer/electrolyte interface, the charge transport characteristics are studied using electrochemical impedance spectroscopy (EIS). The EIS provides the insights into charge separation (photoelectron and photoholes) as well as charge transport (photoelectrons) at Fe_2O_3 or $BiVO_4$/ WO_3 hetero interface as well as Fe_2O_3 or $BiVO_4$/ WO_3 fiber/electrolyte interface [45, 46]. Typical Nyquist plots of PEC cell using Fe_2O_3 and $BiVO_4$ photoanode in the presence and absence of WO_3 backbone fiber layer studied at dark and light irradiation condition is summarized in **Figure 6 (a) and (b), respectively.** The obtained Nyquist plot is simulated with the equivalent circuit shown in the **Figure S4** (see supporting information). In the equivalent circuit, R_s indicates the sheet resistance of the charge collector (FTO), CPE indicates the constant phase element, and R_{ct} indicates the charge transfer resistance at the electrode/electrolyte interface. Under dark condition the diameter of semicircle in Nyquist plot indicates the charge transfer resistance (R_{ct}) i.e. electron transport from outside circuit to the electrolyte. This explain the capability of electron conduction through solid film. For instance, the film possessing high electron conduction results less charge transfer resistance. The estimated charge transfer resistance (R_{ct}) value of WO_3 back bone nanofiber from **Figure 6 (a)** is found to be ~8606 Ω. The

simulated R_{ct} values of Fe_2O_3 and $BiVO_4$ films are found to be 1.54 x10^5 Ω and 1.37 x10^5 Ω, respectively. Surprisingly, the R_{ct} values of Fe_2O_3/WO_3 and $BiVO_4/WO_3$ films are markedly reduced to ~64530 Ω and ~52367 Ω, respectively. It clearly implies that the weak electron transport at Fe_2O_3 and $BiVO_4$ films are improved markedly by highly conducting WO_3 backbone fibers, which in turn reduces the charge transfer resistance. The diameter of the semicircle in **Figure 6 (b)** obtained under applied potential in associate with light irradiation indicates the charge transfer resistance of photocharge carrier separation at electrode/electrolyte interfaces. Here the photoholes transport is also involved in addition to the photoelectrons. Briefly, the photocharge carrier electron and holes could reach the respective terminals. The photoelectrons from conduction band (CB) of photoabsorber (Fe_2O_3 or $BiVO_4$) will transfer to charge collector (FTO). Conversely, the photoholes from valence band (VB) of photoabsorber to the electrolyte (**Figure 7a**). In the case of n type photoabsorbers Fe_2O_3 or $BiVO_4$ they are effectively conducting photoelectrons from CB to charge collector but inadequate in photohole transfer to the electrolyte. From **Figure 6b**, estimated charge transfer resistance value of Fe_2O_3 and $BiVO_4$ is markedly reduced in the presence of WO_3 back bone nanofibers. In particular, R_{ct} value of $BiVO_4$ film is reduced three folds from 10^5 order to 10^2 (inset of **Figure 6 (b)**). This implies that highly interconnected WO_3 back bone nanofibers collect the photoelectrons from point of charge injection at primary photoabsorber Fe_2O_3 or $BiVO_4$ to the charge collector. This enhanced charge collection from Fe_2O_3 or $BiVO_4$ /WO_3 interfaces lead effective charge separation at electrode/electrolyte interfaces.

Further, the photoelectrochemical property of Fe_2O_3 and $BiVO_4$ in the presence and absence of WO_3 films were examined through chronoamperometry plots. Under dark and light condition (on/off), the current generation from PEC cell is recorded and summarized in **Figure 7b**. Comparing the overall photocurrent generation, the WO_3 fiber backbone assisted

Fe_2O_3 and $BiVO_4$ photoanodes showed two-fold higher photocurrent generation compare to that of backbone-free films. As discussed in the impedance analysis, it clearly advocates that backbone fibers facilitate the electron transport to the charge collector and charge separation at Fe_2O_3 and $BiVO_4$ /electrolyte interfaces. Thus, the effective charge separation through fiber backbone, and efficient light harvesting at visible light region results high photocurrent generation at Fe_2O_3 and $BiVO_4$ films compare to WO_3 backbone-free films. Based on the above experimental discussion, the schematic structure of Fe_2O_3 or $BiVO_4$/ WO_3 heterointerface is illustrated in **Figure 7a** [47, 48]. Though the observed photocurrent is lower than that of previous reports on heterostructure photoanodes such as Fe_2O_3/WO_3,[33, 49, 50] and $BiVO_4/WO_3$ [51] [52], which can be improved by increasing the electrode thickness of WO_3 fibrous electrode. It is anticipated that high filling of fibrous network will afford more room for loading primary photoabsorber (Fe_2O_3 or $BiVO_4$). Furthermore, three dimensionally filled WO_3 back bone fiber channels can facilitate the rapid photoelectron transport from the entire electrode to charge collector lead thickness independent photocurrent generation at Fe_2O_3 or $BiVO_4$ films. Therefore, photocurrent results on WO_3 scaffold based films encourages to revisit the photoanode architecture with fibrous backbones instead of directly coated flat type thin films. It is worthy to mention that due to the difference in thickness of the Fe_2O_3/WO_3 and $BiVO_4/WO_3$ electrodes, we couldn't compare the performance between them. However, the heterostrutured Fe_2O_3/WO_3 and $BiVO_4/WO_3$ films showed high photocurrent density and less charge transfer resistance than that of individual Fe_2O_3 and $BiVO_4$ thin films.

4. Conclusion

In conclusion, merits of WO_3 backbone fiber in charge separation and charge transport at Fe_2O_3 and $BiVO_4$ photoanodes were demonstrated. This proof-of-concept based backbone assisted photoanodes showed high light absorbance and charge separation at

electrode/electrolyte interfaces compare to directly coated backbone-free semiconductor films. Furthermore, these highly conductive back bone assisted photoanodes may overcome thickness dependence diffusion length, which need to be studied in detail. In addition, the wide-pore structured fiber-type backbones may support the effective electrolyte percolation at photoanode and can reduce the charge recombination at electrode/electrolyte interfaces. Yet, the conductivity of the WO_3 fibers can be improved by metal doping. It is anticipated that readily available WO_3 fibrous electrodes can be transformed to any other hetero photoabsorbers. The additional coating of co-catalyst [53] will enhance the performance of PEC oxidation reactions, which can be applied solar fuel generation, chemical synthesis and water pollutant treatment applications.

Acknowledgement

One of the lead authors S.P acknowledges Welsh Government and European Regional Development Fund (ERDF) for partial support of this project through Sêr Cymru II-Rising Star Fellowship program (80761-SU-102 (West)).

References

[1] A. Fujishima, K. Honda, Electrochemical Photolysis of Water at a Semiconductor Electrode, Nature, 238 (1972) 37-38.

[2] R. Raja, P. Sudhagar, A. Devadoss, C. Terashima, L.K. Shrestha, K. Nakata, R. Jayavel, K. Ariga, A. Fujishima, Pt-free solar driven photoelectrochemical hydrogen fuel generation using 1T MoS2 co-catalyst assembled CdS QDs/TiO2 photoelectrode, Chemical Communications, 51 (2015) 522-525.

[3] G. Kim, M. Oh, Y. Park, Solar-rechargeable battery based on photoelectrochemical water oxidation: Solar water battery, 6 (2016) 33400.

[4] K. Fuku, K. Sayama, Efficient oxidative hydrogen peroxide production and accumulation in photoelectrochemical water splitting using a tungsten trioxide/bismuth vanadate

photoanode, Chemical Communications, 52 (2016) 5406-5409.

[5] K. Fuku, Y. Miyase, Y. Miseki, T. Funaki, T. Gunji, K. Sayama, Photoelectrochemical Hydrogen Peroxide Production from Water on a WO3/BiVO4 Photoanode and from O2 on an Au Cathode Without External Bias, Chemistry – An Asian Journal, 12 (2017) 1111-1119.

[6] J.M. Kesselman, N.S. Lewis, M.R. Hoffmann, Photoelectrochemical Degradation of 4-Chlorocatechol at TiO2 Electrodes: Comparison between Sorption and Photoreactivity, Environmental Science & Technology, 31 (1997) 2298-2302.

[7] M.S. Koo, K. Cho, J. Yoon, W. Choi, Photoelectrochemical Degradation of Organic Compounds Coupled with Molecular Hydrogen Generation Using Electrochromic TiO2 Nanotube Arrays, Environmental Science & Technology, 51 (2017) 6590-6598.

[8] A. Devadoss, P. Sudhagar, S. Das, S.Y. Lee, C. Terashima, K. Nakata, A. Fujishima, W. Choi, Y.S. Kang, U. Paik, Synergistic Metal–Metal Oxide Nanoparticles Supported Electrocatalytic Graphene for Improved Photoelectrochemical Glucose Oxidation, ACS Applied Materials & Interfaces, 6 (2014) 4864-4871.

[9] A. Devadoss, P. Sudhagar, C. Terashima, K. Nakata, A. Fujishima, Photoelectrochemical biosensors: New insights into promising photoelectrodes and signal amplification strategies, Journal of Photochemistry and Photobiology C: Photochemistry Reviews, 24 (2015) 43-63.

[10] M.G. Walter, E.L. Warren, J.R. McKone, S.W. Boettcher, Q. Mi, E.A. Santori, N.S. Lewis, Solar Water Splitting Cells, Chemical Reviews, 110 (2010) 6446-6473.

[11] P. Sudhagar, T. Song, A. Devadoss, J.W. Lee, M. Haro, S. Gimenez, C. Terashima, V.V. Lysak, J. Bisquert, A. Fujishima, U. Paik, Modulating the interaction between gold and TiO2 nanowires for enhanced solar driven photoelectrocatalytic hydrogen generation, Physical Chemistry Chemical Physics, (2015).

[12] D.K. Bora, A. Braun, E.C. Constable, "In rust we trust". Hematite - the prospective inorganic backbone for artificial photosynthesis, Energy & Environmental Science, 6 (2013)

407-425.

[13] M.J. Katz, S.C. Riha, N.C. Jeong, A.B.F. Martinson, O.K. Farha, J.T. Hupp, Toward solar fuels: Water splitting with sunlight and “rust”?, Coordination Chemistry Reviews, 256 (2012) 2521-2529.

[14] Y. Qiu, S.-F. Leung, Q. Zhang, B. Hua, Q. Lin, Z. Wei, K.-H. Tsui, Y. Zhang, S. Yang, Z. Fan, Efficient Photoelectrochemical Water Splitting with Ultrathin films of Hematite on Three-Dimensional Nanophotonic Structures, Nano Letters, 14 (2014) 2123-2129.

[15] A. Annamalai, P.S. Shinde, A. Subramanian, J.Y. Kim, J.H. Kim, S.H. Choi, J.S. Lee, J.S. Jang, Bifunctional TiO2 underlayer for [small alpha]-Fe2O3 nanorod based photoelectrochemical cells: enhanced interface and Ti4+ doping, Journal of Materials Chemistry A, 3 (2015) 5007-5013.

[16] A. Annamalai, A. Subramanian, U. Kang, H. Park, S.H. Choi, J.S. Jang, Activation of Hematite Photoanodes for Solar Water Splitting: Effect of FTO Deformation, The Journal of Physical Chemistry C, 119 (2015) 3810-3817.

[17] T.W. Kim, K.-S. Choi, Nanoporous BiVO₄ Photoanodes with Dual-Layer Oxygen Evolution Catalysts for Solar Water Splitting, Science, 343 (2014) 990-994.

[18] Q. Jia, K. Iwashina, A. Kudo, Facile fabrication of an efficient BiVO4 thin film electrode for water splitting under visible light irradiation, Proceedings of the National Academy of Sciences, 109 (2012) 11564-11569.

[19] C. Ravidhas, A. Juliat Josephine, P. Sudhagar, A. Devadoss, C. Terashima, K. Nakata, A. Fujishima, A. Moses Ezhil Raj, C. Sanjeeviraja, Facile synthesis of nanostructured monoclinic bismuth vanadate by a co-precipitation method: Structural, optical and photocatalytic properties, Materials Science in Semiconductor Processing, 30 (2015) 343-351.

[20] Y. Yuan, J. Gu, K.-H. Ye, Z. Chai, X. Yu, X. Chen, C. Zhao, Y. Zhang, W. Mai,

Combining Bulk/Surface Engineering of Hematite To Synergistically Improve Its Photoelectrochemical Water Splitting Performance, ACS Applied Materials & Interfaces, 8 (2016) 16071-16077.

[21] R.P. Antony, P.S. Bassi, F.F. Abdi, S.Y. Chiam, Y. Ren, J. Barber, J.S.C. Loo, L.H. Wong, Electrospun Mo-BiVO4 for Efficient Photoelectrochemical Water Oxidation: Direct Evidence of Improved Hole Diffusion Length and Charge separation, Electrochimica Acta, 211 (2016) 173-182.

[22] A.J.E. Rettie, H.C. Lee, L.G. Marshall, J.-F. Lin, C. Capan, J. Lindemuth, J.S. McCloy, J. Zhou, A.J. Bard, C.B. Mullins, Combined Charge Carrier Transport and Photoelectrochemical Characterization of BiVO4 Single Crystals: Intrinsic Behavior of a Complex Metal Oxide, Journal of the American Chemical Society, 135 (2013) 11389-11396.

[23] H.S. Park, K.E. Kweon, H. Ye, E. Paek, G.S. Hwang, A.J. Bard, Factors in the Metal Doping of BiVO4 for Improved Photoelectrocatalytic Activity as Studied by Scanning Electrochemical Microscopy and First-Principles Density-Functional Calculation, The Journal of Physical Chemistry C, 115 (2011) 17870-17879.

[24] Y. Ling, Y. Li, Review of Sn-Doped Hematite Nanostructures for Photoelectrochemical Water Splitting, Particle & Particle Systems Characterization, 31 (2014) 1113-1121.

[25] C. Du, J. Wang, X. Liu, J. Yang, K. Cao, Y. Wen, R. Chen, B. Shan, Ultrathin CoOx-modified hematite with low onset potential for solar water oxidation, Physical Chemistry Chemical Physics, 19 (2017) 14178-14184.

[26] J.H. Kim, G. Magesh, H.J. Kang, M. Banu, J.H. Kim, J. Lee, J.S. Lee, Carbonate-coordinated cobalt co-catalyzed BiVO4/WO3 composite photoanode tailored for CO2 reduction to fuels, Nano Energy, 15 (2015) 153-163.

[27] J. Choi, P. Sudhagar, J.H. Kim, J. Kwon, J. Kim, C. Terashima, A. Fujishima, T. Song, U. Paik, WO3/W:BiVO4/BiVO4 graded photoabsorber electrode for enhanced

photoelectrocatalytic solar light driven water oxidation, Physical Chemistry Chemical Physics, 19 (2017) 4648-4655.

[28] F. Le Formal, N. Tetreault, M. Cornuz, T. Moehl, M. Gratzel, K. Sivula, Passivating surface states on water splitting hematite photoanodes with alumina overlayers, Chemical Science, 2 (2011) 737-743.

[29] C. Du, M. Zhang, J.-W. Jang, Y. Liu, G.-Y. Liu, D. Wang, Observation and Alteration of Surface States of Hematite Photoelectrodes, The Journal of Physical Chemistry C, 118 (2014) 17054-17059.

[30] M.N. Shaddad, M.A. Ghanem, A.M. Al-Mayouf, S. Gimenez, J. Bisquert, I. Herraiz-Cardona, Cooperative Catalytic Effect of ZrO2 and α-Fe2O3 Nanoparticles on BiVO4 Photoanodes for Enhanced Photoelectrochemical Water Splitting, ChemSusChem, 9 (2016) 2779-2783.

[31] A. Malathi, V. Vasanthakumar, P. Arunachalam, J. Madhavan, M.A. Ghanem, A low cost additive-free facile synthesis of BiFeWO6/BiVO4 nanocomposite with enhanced visible-light induced photocatalytic activity, Journal of Colloid and Interface Science, 506 (2017) 553-563.

[32] S. Kment, F. Riboni, S. Pausova, L. Wang, L. Wang, H. Han, Z. Hubicka, J. Krysa, P. Schmuki, R. Zboril, Photoanodes based on TiO2 and [small alpha]-Fe2O3 for solar water splitting - superior role of 1D nanoarchitectures and of combined heterostructures, Chemical Society Reviews, 46 (2017) 3716-3769.

[33] K. Sivula, F.L. Formal, M. Grätzel, WO3−Fe2O3 Photoanodes for Water Splitting: A Host Scaffold, Guest Absorber Approach, Chemistry of Materials, 21 (2009) 2862-2867.

[34] P.M. Rao, L. Cai, C. Liu, I.S. Cho, C.H. Lee, J.M. Weisse, P. Yang, X. Zheng, Simultaneously Efficient Light Absorption and Charge Separation in WO3/BiVO4 Core/Shell Nanowire Photoanode for Photoelectrochemical Water Oxidation, Nano Letters,

14 (2014) 1099-1105.

[35] T. Zhang, J. Su, L. Guo, Morphology engineering of WO3/BiVO4 heterojunctions for efficient photocatalytic water oxidation, CrystEngComm, 18 (2016) 8961-8970.

[36] S.Y. Chae, C.S. Lee, H. Jung, O.-S. Joo, B.K. Min, J.H. Kim, Y.J. Hwang, Insight into Charge Separation in WO3/BiVO4 Heterojunction for Solar Water Splitting, ACS Applied Materials & Interfaces, 9 (2017) 19780-19790.

[37] T. Zhang, J. Su, L. Guo, Hierarchical architecture of WO3 nanosheets by self-assembly of nanorods for photoelectrochemical applications, CrystEngComm, 18 (2016) 665-669.

[38] T. Zhang, Z. Zhu, H. Chen, Y. Bai, S. Xiao, X. Zheng, Q. Xue, S. Yang, Iron-doping-enhanced photoelectrochemical water splitting performance of nanostructured WO3: a combined experimental and theoretical study, Nanoscale, 7 (2015) 2933-2940.

[39] O. Monfort, T. Roch, M. Gregor, L. Satrapinskyy, D. Raptis, P. Lianos, G. Plesch, Photooxidative properties of various BiVO4/TiO2 layered composite films and study of their photocatalytic mechanism in pollutant degradation, Journal of Environmental Chemical Engineering, 5 (2017) 5143-5149.

[40] F.M. Toma, J.K. Cooper, V. Kunzelmann, M.T. McDowell, J. Yu, D.M. Larson, N.J. Borys, C. Abelyan, J.W. Beeman, K.M. Yu, J. Yang, L. Chen, M.R. Shaner, J. Spurgeon, F.A. Houle, K.A. Persson, I.D. Sharp, Mechanistic insights into chemical and photochemical transformations of bismuth vanadate photoanodes, Nature Communications, 7 (2016) 12012.

[41] J.H. Kim, Y.H. Jo, J.H. Kim, J.S. Lee, Ultrafast fabrication of highly active BiVO4 photoanodes by hybrid microwave annealing for unbiased solar water splitting, Nanoscale, 8 (2016) 17623-17631.

[42] X. Zhao, W. Luo, J. Feng, M. Li, Z. Li, T. Yu, Z. Zou, Quantitative Analysis and Visualized Evidence for High Charge Separation Efficiency in a Solid-Liquid Bulk Heterojunction, Advanced Energy Materials, 4 (2014) 1301785-n/a.

[43] S.J. Hong, S. Lee, J.S. Jang, J.S. Lee, Heterojunction BiVO4/WO3 electrodes for enhanced photoactivity of water oxidation, Energy & Environmental Science, 4 (2011) 1781-1787.

[44] M. Alexander, K. Ilina, F. Alena, F.-R. Dina, B. Thomas, S. Christina, Dual absorber Fe_2O_3 /WO_3 host-guest architectures for improved charge generation and transfer in photoelectrochemical applications, Materials Research Express, 4 (2017) 016409.

[45] B. Klahr, S. Gimenez, F. Fabregat-Santiago, J. Bisquert, T.W. Hamann, Photoelectrochemical and Impedance Spectroscopic Investigation of Water Oxidation with "Co–Pi"-Coated Hematite Electrodes, Journal of the American Chemical Society, 134 (2012) 16693-16700.

[46] L. Bertoluzzi, P. Lopez-Varo, J.A. Jimenez Tejada, J. Bisquert, Charge transfer processes at the semiconductor/electrolyte interface for solar fuel production: insight from impedance spectroscopy, Journal of Materials Chemistry A, 4 (2016) 2873-2879.

[47] I. Grigioni, K.G. Stamplecoskie, E. Selli, P.V. Kamat, Dynamics of Photogenerated Charge Carriers in WO3/BiVO4 Heterojunction Photoanodes, The Journal of Physical Chemistry C, 119 (2015) 20792-20800.

[48] S. Hosseini, E. Eftekhari, S.M. Soltani, F.E. Babadi, L.J. Minggu, M.H.S. Ismail, Synthesis, characterization and performance evaluation of three-layered photoanodes by introducing a blend of WO3 and Fe2O3 for dye degradation, Applied Surface Science, 289 (2014) 53-61.

[49] Enhanced Water Oxidation Photoactivity of Nano-Architectured α-Fe2O3–WO3 Composite Synthesized by Single-Step Hydrothermal Method, Journal of Electronic Materials, (2018).

[50] Y. Li, L. Zhang, R. Liu, Z. Cao, X. Sun, X. Liu, J. Luo, WO3@α-Fe2O3 Heterojunction Arrays with Improved Photoelectrochemical Behavior for Neutral pH Water Splitting,

ChemCatChem, 8 (2016) 2765-2770.

[51] J. Su, L. Guo, N. Bao, C.A. Grimes, Nanostructured WO3/BiVO4 Heterojunction Films for Efficient Photoelectrochemical Water Splitting, Nano Letters, 11 (2011) 1928-1933.

[52] Y. Pihosh, I. Turkevych, K. Mawatari, J. Uemura, Y. Kazoe, S. Kosar, K. Makita, T. Sugaya, T. Matsui, D. Fujita, M. Tosa, M. Kondo, T. Kitamori, Photocatalytic generation of hydrogen by core-shell WO3/BiVO4 nanorods with ultimate water splitting efficiency, Scientific Reports, 5 (2015) 11141.

[53] S.K. Pilli, R. Janarthanan, T.G. Deutsch, T.E. Furtak, L.D. Brown, J.A. Turner, A.M. Herring, Efficient photoelectrochemical water oxidation over cobalt-phosphate (Co-Pi) catalyst modified BiVO4/1D-WO3 heterojunction electrodes, Physical Chemistry Chemical Physics, 15 (2013) 14723-14728.

Figures legends

Figure 1. Schematic illustration of Fe_2O_3 or $BiVO_4$ semiconductor film synthesising (a) directly onto substrate and (b) WO_3 fibrous pre-coated substrate by spin coating.

Figure 2. (a) XRD result of WO_3 fiber, Fe_2O_3 and $BiVO_4$ films in the presence and absence of WO_3 fibers. Note that the crystalline contribution from FTO substrate is indicated in * symbol.

Figure 3. SEM images of (a) Fe_2O_3 thin film, (b) $BiVO_4$ thin film, (c) WO_3 nanofibers, (d) Fe_2O_3 coated WO_3 nanofiber, and (e) $BiVO_4$ coated WO_3 nanofiber coated on FTO glass substrates.

Figure 4. HRTEM images of $BiVO_4/WO_3$ sample (a) at 50 nm scale and (b) at 10 nm scale.

Figure 5. (a) Optical absorbance spectra of Fe_2O_3 and $BiVO_4$ films in the presence and absence of WO_3 fiber, (b) Optical reflectance spectra of Fe_2O_3/WO_3 and $BiVO_4/WO_3$ composite fibers compared with WO_3 fiber film (note that films are coated onto FTO substrate).

Figure 6. Nyquist plots of PEC cells consisted with different photoanodes measured at (a) under dark condition and (b) Light irradiation condition (100 $mWcm^{-2}$). Note that the measurements were carried out at operating potential 0.7 V vs Ag/AgCl)

Figure 7. (a) Proposed energetic structure of Fe_2O_3/WO_3 and $BiVO_4/WO_3$ heterointerfaces at photoelectrocatalytic water oxidation performance and (b) Chronoamperometry plots of PEC cell with different photoanodes (measurements carried out at applied potential 0.7 V vs Ag/AgCl). Note that 0.5 M of aqueous Na_2SO_4 is used as electrolyte. The photocurrent measured under light irradiation is obtained at light intensity AM 1.5 (100 $mWcm^{-2}$).

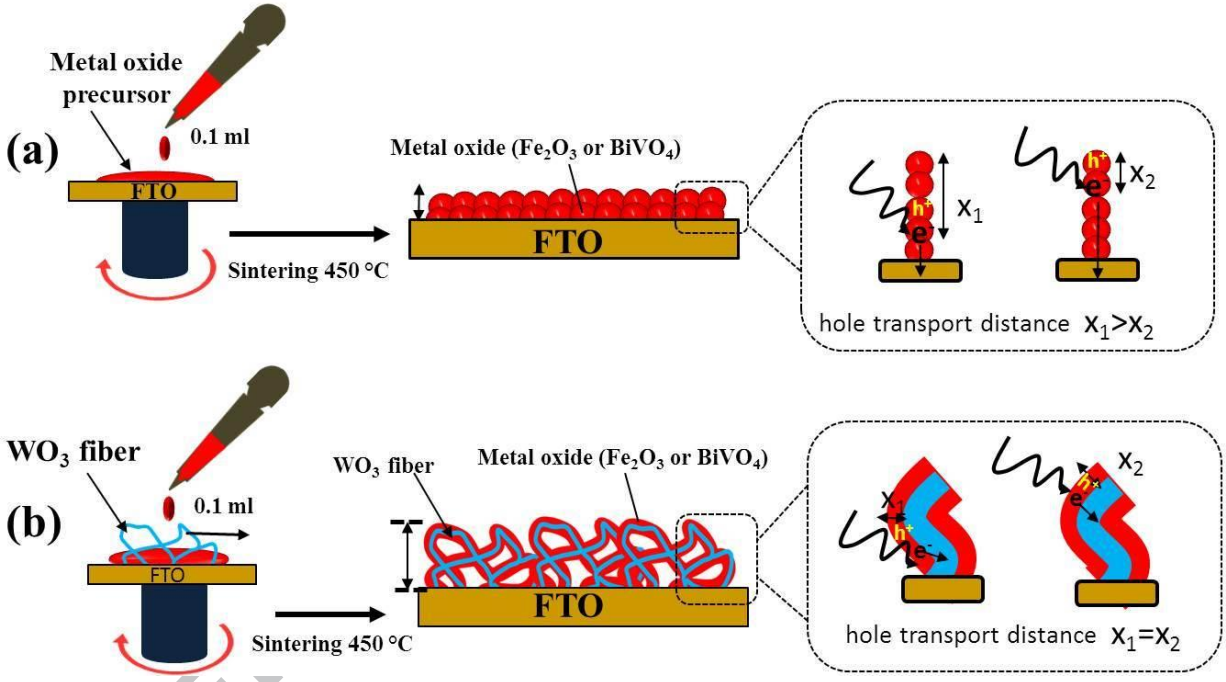

Figure 1.

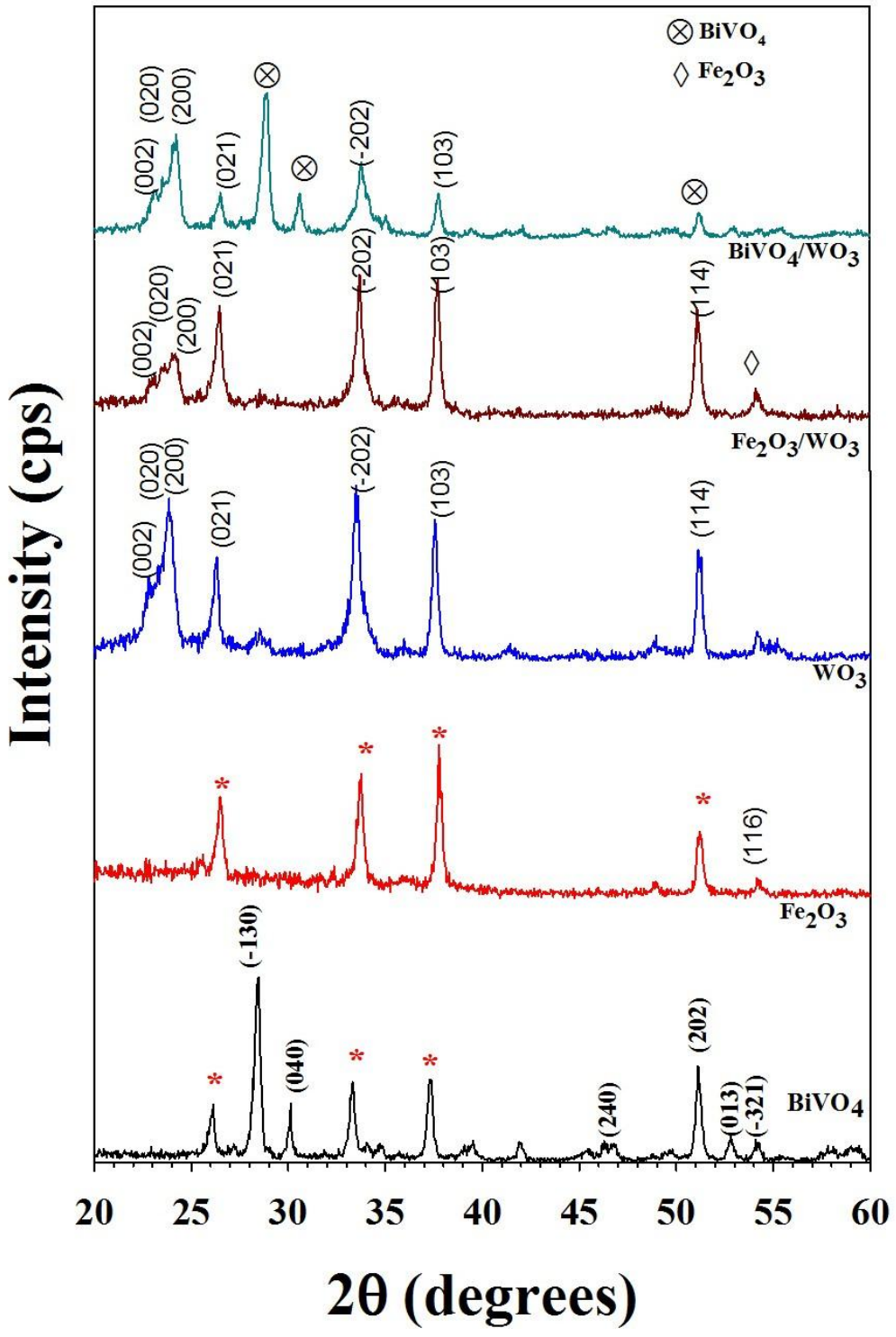
⊗ BiVO4
◊ Fe2O3
(002)
(020)
(200)
(021)
(-202)
(103)
(114)
(116)
(-130)
(040)
(240)
(013)
(-321)
BiVO4/WO3
Fe2O3/WO3
WO3
Fe2O3
BiVO4
Intensity (cps)
20
25
30
35
40
45
50
55
60
2θ (degrees)

Figure 2.

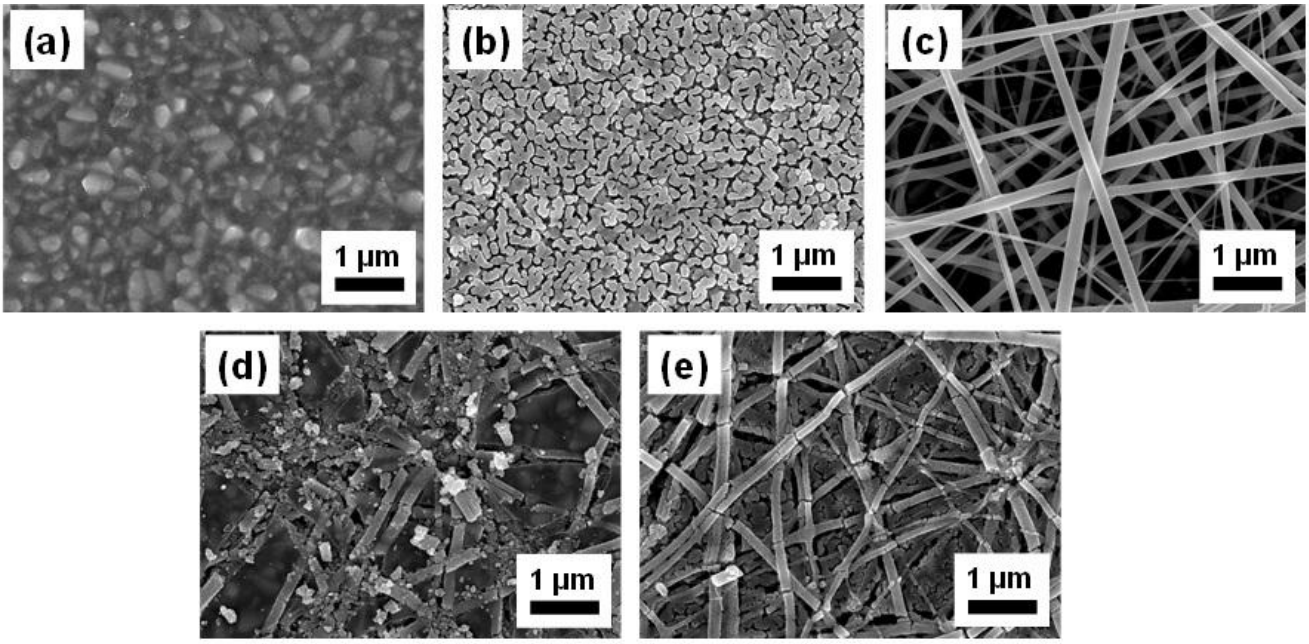

Figure 3.

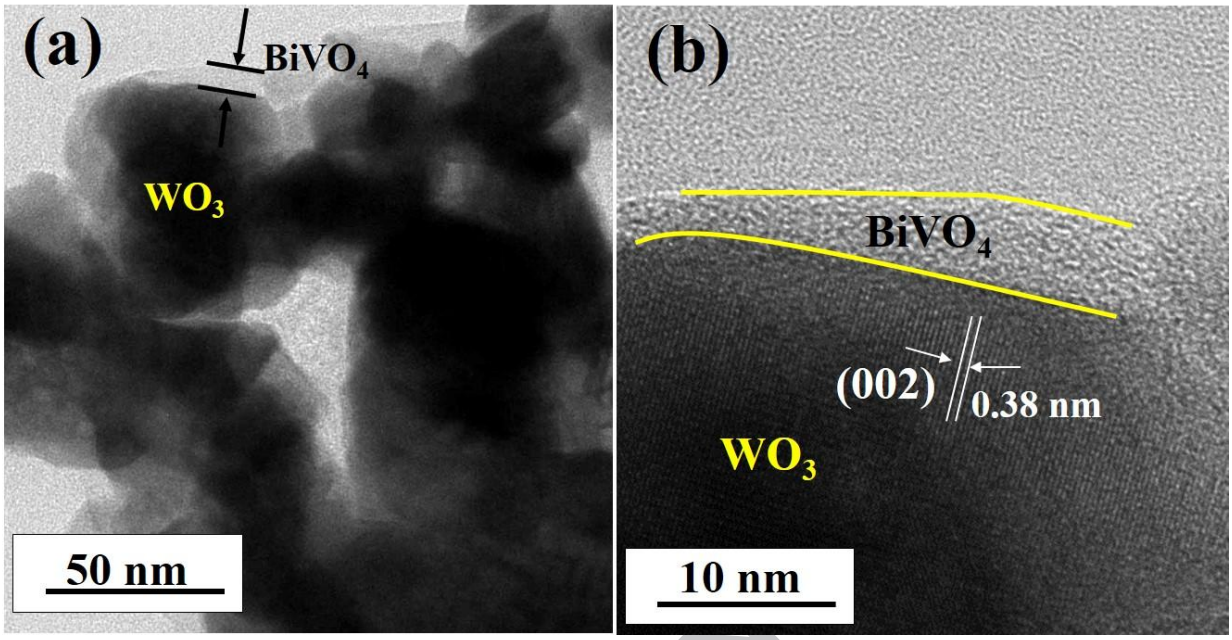

Figure 4

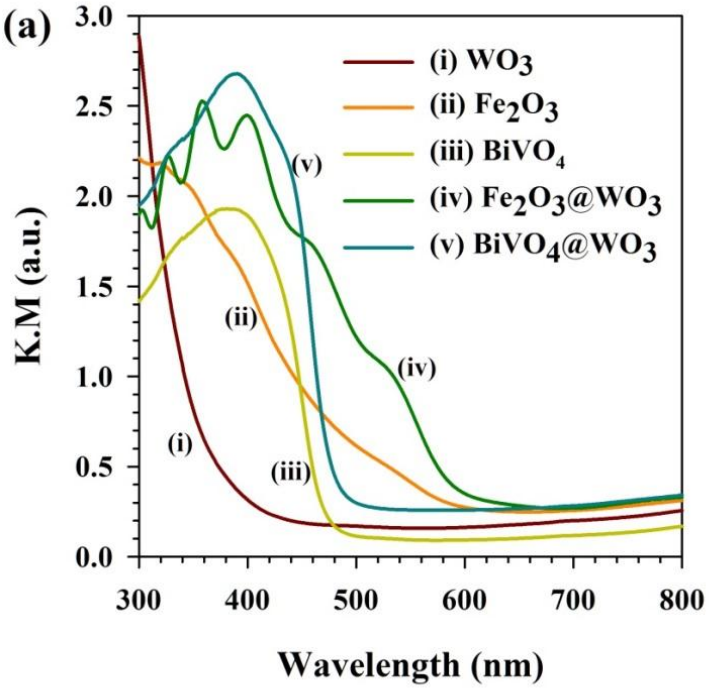

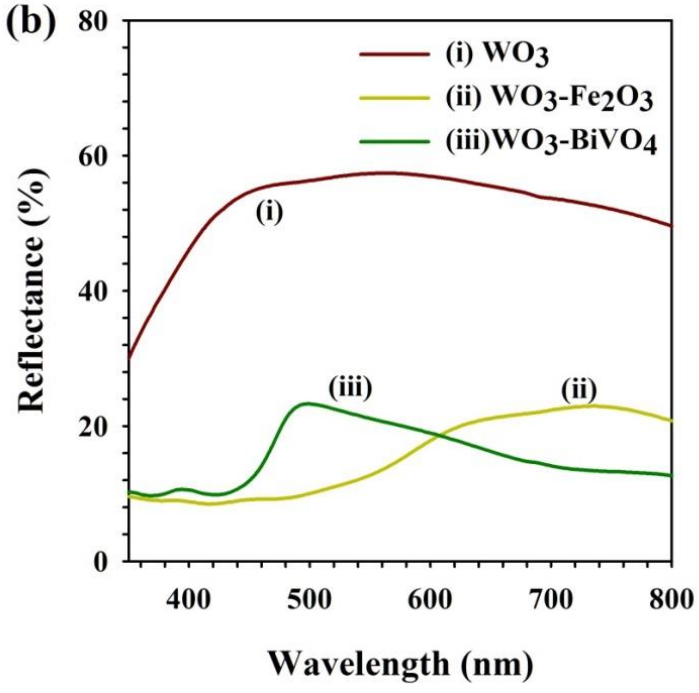

Figure 5.

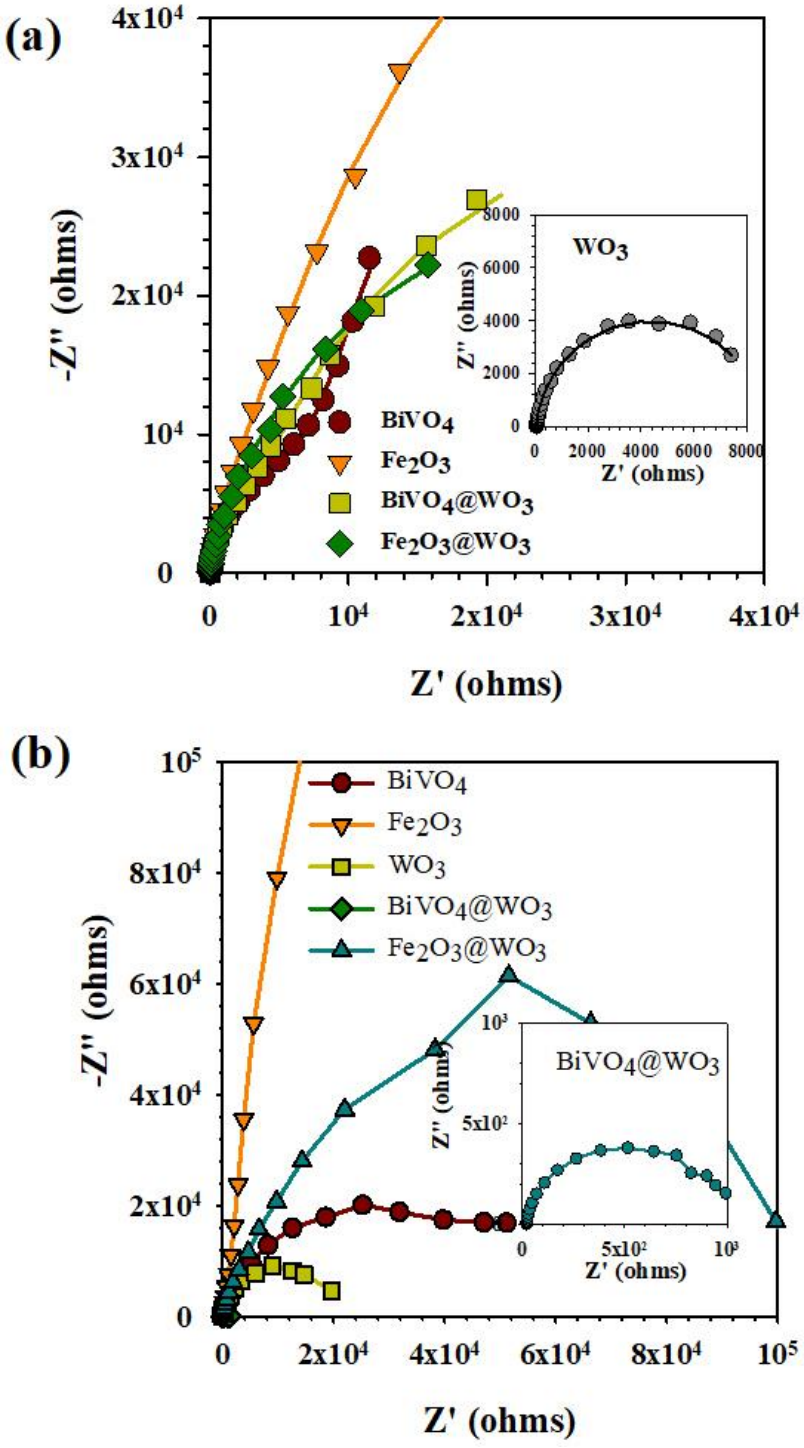
(a)
4x10⁴
3x10⁴
2x10⁴
10⁴
0
-Z'' (ohms)
0
10⁴
2x10⁴
3x10⁴
4x10⁴
Z' (ohms)
BiVO4
Fe2O3
BiVO4@WO3
Fe2O3@WO3
WO3
8000
6000
4000
2000
0
Z'' (ohms)
0
2000
4000
6000
8000
Z' (ohms)
(b)
10⁵
8x10⁴
6x10⁴
4x10⁴
2x10⁴
0
-Z'' (ohms)
0
2x10⁴
4x10⁴
6x10⁴
8x10⁴
10⁵
Z' (ohms)
BiVO4
Fe2O3
WO3
BiVO4@WO3
Fe2O3@WO3
10³
5x10²
Z'' (ohms)
0
5x10²
10³
Z' (ohms)

Figure 6

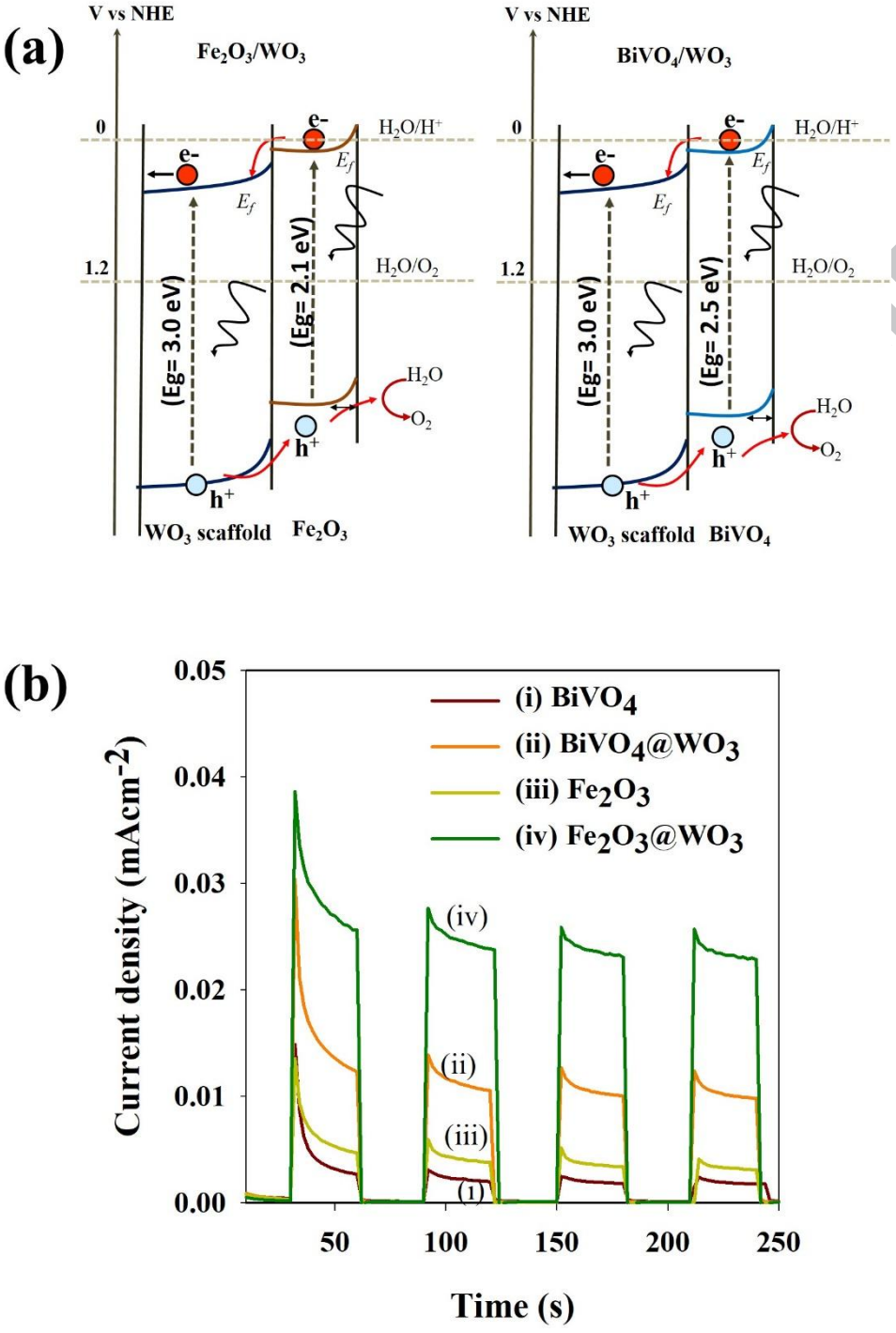
(a)
V vs NHE
Fe_2O_3/WO_3
0
1.2
H_2O/H^+
H_2O/O_2
e-
E_f
(Eg= 3.0 eV)
(Eg= 2.1 eV)
H_2O
O_2
h^+
WO_3 scaffold
Fe_2O_3
V vs NHE
$BiVO_4/WO_3$
(Eg= 2.5 eV)
WO_3 scaffold
$BiVO_4$
(b)
Current density ($mAcm^{-2}$)
Time (s)
(i) $BiVO_4$
(ii) $BiVO_4$@WO_3
(iii) Fe_2O_3
(iv) Fe_2O_3@WO_3
0.05
0.04
0.03
0.02
0.01
0.00
50
100
150
200
250

Figure 7

Highlights

- Electrospinning derived WO_3 fibrous is demonstrated as backbone scaffold in light driven photoanode.
- Synthesis route of sol-gel assisted spin coated Fe_2O_3 and $BiVO_4$ thin films onto WO_3 fibers is demonstrated.
- High visible light harvesting is achieved at Fe_2O_3 and $BiVO_4$ through introducing WO_3 nanofibrous backbone scaffold.
- Charge transport and charge separation at Fe_2O_3/WO_3 and $BiVO_4/WO_3$ based heterostructured photoanode/electrolyte interfaces is promoted.
- Underlying mechanism of one dimensional WO_3 fibrous backbone scaffold assisted photoanode in solar fuel generation is examined.

Graphical abstract